SOL-GEL PREPARATION AND SINTERING OF AL, FE, SI MIXED OXIDES DOPED CERIA

M. Escalante *[a], G. González [b,c]

[a] Departamento de Ciencia de los Materiales, Universidad Simón Bolívar, Caracas, Venezuela.
[b] School of Physical Sciences and Nanotechnology, Yachay Tech University, Urcuquí, Ecuador
[c] Centro de Ing Materiales y Nanotecnología, Instituto Venezolano de Investigaciones Científicas, IVIC, Caracas, Venezuela

*E-mail: mesca07@gmail.com

ABSTRACT
Undoped CeO2, co-doped and tri-doped CeO2 with Si, Si-Al and Si-Fe, were prepared by sol-gel method. Nanoparticles with an average crystal size of 2-10 nm, were obtained and structurally characterized by X-Ray Diffraction (XRD), Scanning Electron Microscopy (SEM) and Transmission Electron Microscopy (TEM). Powders were compacted by uniaxial pressure and sintered in air at 1250 °C to obtained sintered pellets. The different compositions maintained the cerianite crystal structure, implying that dopant elements enter in the structure forming a solid solution, although some segregation was observed by SEM and TEM analysis in pellets. The undoped CeO2 material reached a relative density of 0.95% at 1250°C while doped samples presented variations in this value and grain size and relative density, clearly attributed to doping. According to these results, these materials could have potential applications in solid oxide fuel cells, electrodes and sensors.

Keywords: multi-doped ceria, solid oxide fuel cells, aluminium, iron, silicon.

Síntesis sol-gel y sinterización de ceria dopada con óxidos mixtos de Al, Fe y Si

RESUMEN
Se prepararon polvos de ceria (CeO$_2$), ceria codopada con Si, ceria tridopada con Si-Al y Si-Fe Fe mediante el método sol-gel. Se obtuvieron nanopartículas con un tamaño medio de cristal de 2-10 nm y se caracterizaron estructuralmente por Difracción de Rayos X (DRX), Microscopía Electrónica de Barrido (MEB) y Microscopía Electrónica de Transmisión (MET). Los polvos se compactaron mediante presión uniaxial y se sinterizaron en aire a 1250 °C para obtener gránulos sinterizados. Las diferentes composiciones mantuvieron la estructura cristalina de cerianita, lo que implica que los elementos dopantes entran en la estructura formando una solución sólida, aunque se observó cierta segregación mediante análisis SEM y TEM en los pellets. El material CeO$_2$ sin dopar alcanzó una densidad relativa del 0,95% a 1250°C, mientras que las muestras dopadas presentaron variaciones en este valor y en el tamaño de grano y la densidad relativa, claramente atribuidas al dopaje. Según estos resultados, estos materiales podrían tener aplicaciones potenciales en pilas de combustible de óxido sólido, así como de electrodos y sensores.

Palabras claves: ceria multidopada, celdas de óxido sólido, aluminio, hierro, silicio.

INTRODUCTION

For a long time, yttria-stabilized zirconia (YSZ) has been a wildly used electrolyte material for solid oxide fuel cells (SOFCs), because of its high stability and ionic conductivity at high temperature (>800 °C) [1–7] . However, the high temperature environment involves several critical disadvantages including: the accelerated degradation of cell components; slow start-up time which increase the energy consumption making the process less efficient; and limited selection of materials in terms of mechanical and chemical compatibility [7–9]. Those factors impede its commercialization in SOFC technology and motivate to explore other alternatives more efficient and reliables [10,11]. Ceria (cerium oxide, CeO2) is a cubic fluorite-type oxide, considered one of the most important ceramic oxides [12–16]. When ceria is doped with heterovalent cations such as rare earth, typically gadolinium (Gd) and samarium (Sm) [17,18], it shown a robust chemical stability [19–21] and superior

oxygen ion conductivity at moderate temperatures [22–24] compared to YSZ, which makes of this compound a promising candidate for electrolytes material in SOFCs applications. Also, it can be easily obtained by different synthesis methods [25–29]: hydrothermal synthesis [30,31], jet pyrolysis [32], inverse microemulsions method [33], combustion [14] and sonochemical synthesis [34], and sol-gel [35,36]. The latter is commonly used for the synthesis of cathodes and solid electrolytes in SOFCs [28,37,38].

Recent researches in the field of SOFCs [39–42] has focused on developing efficient materials but with easier and more economical manufacturing processes. Unlike tradicional dopants such as Gd and Sm, doping with alkaline earth metal ions as aluminum (Al) and iron (Fe) [43–45] enhance the ionic conductivity of ceria while simultaneously improving its chemical stability and reducing costs. The sol-gel process is highly adaptable and versatile, and it´s considered an effective chemical route, because it doesn't require high temperatures, and allow obtaining ultrafine pure powders [35–37,46] with nanometric characteristics with several composition ranges [16]. Therefore, the present work studies the effect of doping, co-doping and tri-doping ceria (with Si, Si-Al, Si-Fe and Si-Al-Fe) were prepared by using the sol-gel method. The effect of the doping element on the structural properties has been discussed.

EXPERIMENTAL, MATERIALS AND METHODS

The following Sigma Aldrich chemical reagents were used for the synthesis of doped cerianites: cerium oxide (CeO_2), with 99.9%, hexahydrate aluminum chloride ($AlCl_3 6H_2O$) 0.07 – 0.30 % mol, ferric oxide (Fe_2O_3) 0.04 – 0.14 % mol and tetraethylorthosilicate (TEOS) $Si(OC_2H_5)_4$ as 0.010 – 0.012 % mol as precursor. Sol-gel in basic medium (pH > 10) was the chemical methodology employed to synthesize the ceramic powders. For this, each compound was dissolved in aqueous media with H_2SO_4, HCl and/or HNO_3 1M, 2M and 1M, respectively. Then, they were mixed with NH_4Cl and NH_4OH to obtain different hydroxides: $Ce(OH)_4$, $Al(OH)_3$, $Fe(OH)_3$ and $Si(OH)_4$.

These hydroxides were combined with each other and with TEOS according to Table 1 and to acquire different oxide ceria compositions. Afterward, they ware centrifuged at 25 rpm during 8 minutes in distilled water in a Damon IEC Model K centrifuge until pH = 7, filtered and dried at 100°C during 5 hours. Consolidation of the ceramic powders was done by preparing disks of 1,24 cm^2 pressed under uniaxial pressure (load of 700 - 800 KN) and finally sintered at 1250 °C for 12h in a tubular furnace to obtain solid ceramics disks.

Table 1. Sample Compositional Nomenclature of doped cerianites.

MIXTURE	DOPED COMPOSITION	DESIGNATION
$Ce(OH)_4$	CeO_{2-x}	CeO_2
$Ce(OH)_4$ + TEOS	$Ce_\alpha Si_{1-\alpha} O_{2-x}$	CeSi
$Ce(OH)_4$ + TEOS + $Al(OH)_3$	$Ce_\alpha Si_\beta Al_\gamma O_{2-x}$	CeSiAl
$Ce(OH)_4$ + TEOS + $Fe(OH)_3$	$Ce_\alpha Si_\beta Fe_\delta O_{2-x}$	CeSiFe
$Ce(OH)_4$ + TEOS + $Al(OH)_3$ + $Fe(OH)_3$	$Ce_\alpha Si_\beta Al_{3\gamma} Fe_\delta O_{2-x}$	CeSi3AlFe
$Ce(OH)_4$ + TEOS + $Al(OH)_3$ + $Fe(OH)_3$	$Ce_\alpha Si_\beta Al_\gamma Fe_{3\delta} O_{2-x}$	CeSiAl3Fe

Powders and ceramic disks were characterized by X-ray diffraction (XRD), scanning electron microscopy (SEM) and transmission electron microscopy (TEM). XRD was carried out with a Siemens D5005 diffractometer with Cu Kα radiation (λ=1.540498Å) operated at 40kV and 20mA in the 2θ range of 20°–80° with a step size 0.02 ° and a step time for 2s. Identification of XRD peaks was carried out by JCPDS database. Scherer equation was used to calculate the crystallite size of the nano particles and is given by $D = K\lambda / \beta\cos\theta$; where D is crystallite size, K is the Scherrer constant (K = 0.9), λ is the wavelength of X–rays, β is the full width at half maximum intensity corrected with the instrumental width, and θ is the angle of the main reflection (111). The lattice parameter (*a*) was determined using the CelRef software[47].

SEM images were obtained using a FEI INSPECT F50 FEG microscope operated at 2-5 kV. Characterization by this technique included secondary electron images (SEI) for powders and backscattered electron images (BEI) for the cerianites pellets. Elementary analysis was conducted by X-ray Energy Dispersion (EDX) in order to examine the experimental chemical composition of doped cerianites, and phase composition and grain area analyses were done using ImageJ software [48.] Relative porosity (RP), relative density (RD) of the sintered disks were measured via the Archimedes method in water bath. TEM was performed in a TECNAI FEI Spirit microscope operating at 120 kV and equipped with a LaB6 source

POWDER´S CHARATERIZATION RESULTS AND DISCUSSION

X-ray diffraction

Figure 1 shows the diffractogram of CeO_2, used as control sample. Seven sharp reflections are observed; the most intense correspond to the main peaks of the cubic fluorite structure Fm3m symmetry: (111), (200), (220) and (311), following JCPDS card No. 00-045-1002. This result confirms that the undoped is constituted of a single crystalline phase of cerianite, as expected [33,34].
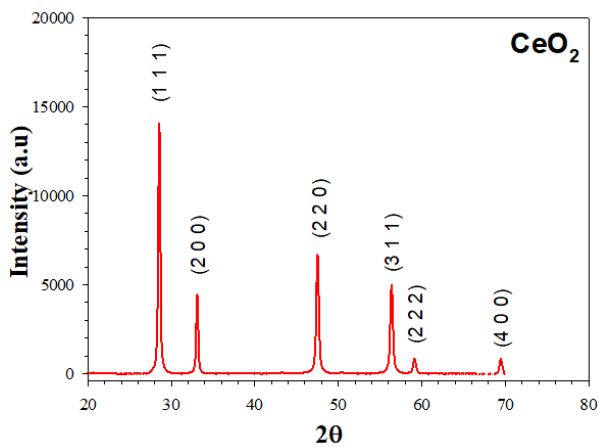
Fig. 1. Powder X-ray diffraction patterns of undoped CeO_2 powders synthesized by the sol - gel method

Figure 2 shows diffractograms of pure CeO_2 sample (Fig 2a) and Al, Fe and Si doped cerianite (Fig 2b). The main

peaks of the doped samples match with control sample, suggesting that CeO_2 is the only single phase obtained. Nevertheless, the peaks in the doped samples are broader and less intense due to the presence of nanometric particles [49–52]. Also, lattice constant (*a*) and crystallite size (*D*) values are presented in table 2.
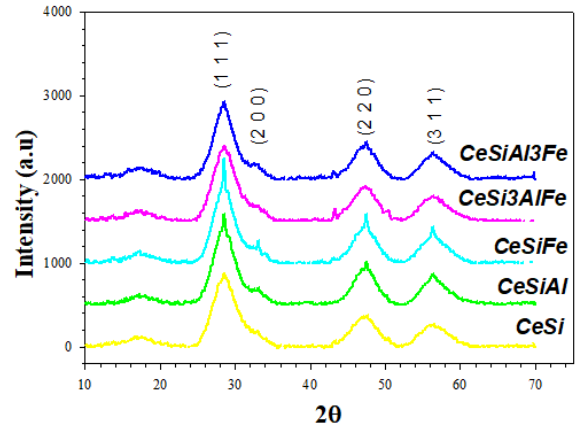
Fig. 2. Powder X-ray diffraction patterns of doped CeO_2 samples: CeSi, CeSiAl, CeSiFe, CeSi3AlFe y CeSiAl3Fe samples synthetized by sol – gel method.

Table 2. Crystallite size and lattice parameter of undoped and doped cerianite samples.

SAMPLE	D (NM)	*a* (Å) SYNTHESIZED POWDERS
CeO_2	25.6	5.423 ± 0.012
CeSi	2.9	5.387 ± 0.028
CeSiAl	3.4	5.408 ± 0.028
CeSiFe	4.4	5.418 ± 0.088
CeSi3AlFe	2.8	5.415 ± 0.033
CeSiAl3Fe	3.6	5.411 ± 0.097

Then, it was found that the crystallite size (*D)* of undoped ceria has a value of 25.6 nm, while for the doped samples this value decreases one order of magnitude between 2.8 - 4.4 nm. This indicates that the doping elements decrease the crystallite size, as has been reported [53,54]. Ouzouit et al [15] also confirmed that sol-gel route produced a small size crystallites compared to others routes. This fact is relevant because nanocrystalline powders are well known to provide faster densification kinetics and lower sintering temperatures [55].

Lattice parameter of the doped samples is modified for doped samples around 5.4 Å. This variation observed of *a*

of 0.5 to 0.6 percent in doped samples respect to undoped one is directly correlated with doping sizes elements and its concentration [14,15,50]. In this study, the difference size of Al^{3+} (0.57 Å), Fe^{3+} (0.67 Å), and Si^{+4} (0.39 Å) cations compared to Ce^{4+} cation (0.92 °A), causes a decreasing of lattice constant that obeys Vegard's Law [56,57]. These dopants also generate structural defects in the anionic subnetwork of ceria that alters its electronic density, producing changes in oxide properties [58,59].

For example, the introduction of Al^{+3}, Fe^{+3} and Si^{4+} cations in the structure of CeO_2 is achieved by the O-vacancy formation mechanism [57], in accordance to the theoretical equilibrium expressed in Kröger-Vink notation (Eq. 1, 2, 3, 4 and 5).

$$Al_2O_3 \xrightarrow{2CeO_2} 2Al'_{Ce} + 3O_O + V_O^{\circ\circ} \qquad \boldsymbol{Eq.\,1}$$

$$Fe_2O_3 \xrightarrow{2CeO_2} 2Fe'_{Ce} + 3O_O + 2V_O^{\circ\circ} \qquad \boldsymbol{Eq.\,2}$$

$$FeO \xrightarrow{CeO_2} Fe''_{Ce} + 2O_O + V_O^{\circ\circ} \qquad \boldsymbol{Eq.\,3}$$

$$SiO_2 \xrightarrow{CeO_2} Si^x_{Ce} + 2O_O \qquad \boldsymbol{Eq.\,4}$$

$$SiO_2 \xrightarrow{CeO_2} 2Si^x_{Ce} + 2O_O + V_O^{\circ\circ} \qquad \boldsymbol{Eq.\,5}$$
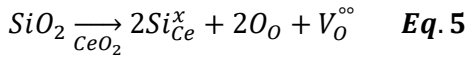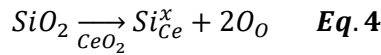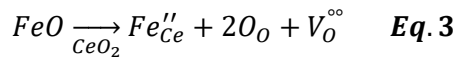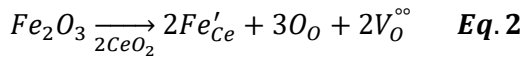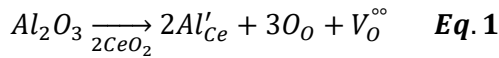
Oxygen vacancies formed could act as preferential nucleation sites, promoting seeding events with disturbing crystallite growth process [60], as is pointed out by Min et al [61]. This also could explain variation of D between doped and undoped samples obtained from XDR results (table 2). Finally, note that it is assumed that Si^{4+} substitutes Ce^{4+} without generating VOs because both ions have the same state valence. However, in some cases silicon doping can generate VOs to balance the additional electronic density in CeO2 structure due to interaction with other defects in the lattice [62,63]

Scanning Electronic Microscopy

SEM images of undoped and doped samples are shown in Figure 3 to Figure 8 with their respective particle sizes

histograms. Table 4 presents their chemical formulas calculated from EDS results, compared with theoretical ones. Additionally, the average agglomerate size (S_A) determined from histograms are reported.
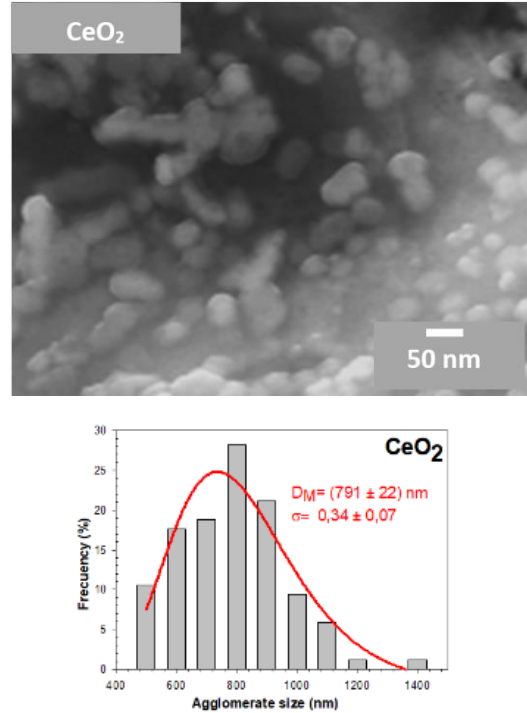
Fig. 3. SEM Images of undoped ceria taken in SEI mode with its respective agglomerate size distribution histogram.
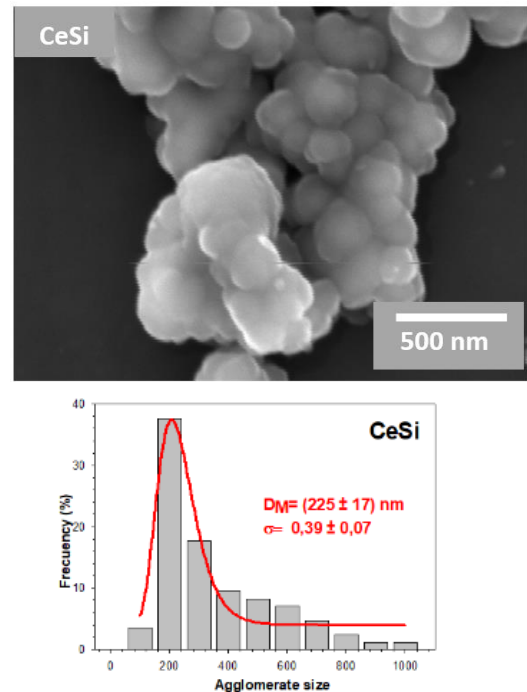
Fig. 4. SEM Images of CeSi sample taken in SEI mode with its respective agglomerate size distribution histogram.
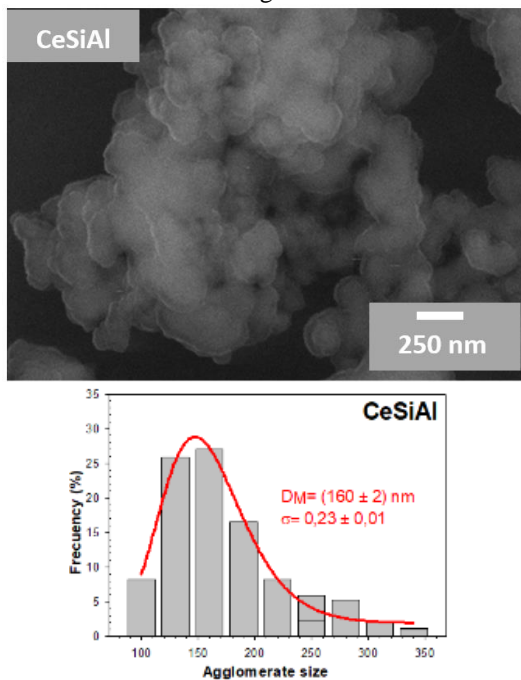
Fig. 5. SEM Images of CeSiAl sample taken in SEI mode with its respective agglomerate size distribution histogram.

Fig. 7. SEM Images of CeSi3AlFe sample taken in SEI mode with its respective agglomerate size distribution histogram.

Fig. 6. SEM Images of CeSiFe sample taken in SEI mode with its respective agglomerate size distribution histogram.
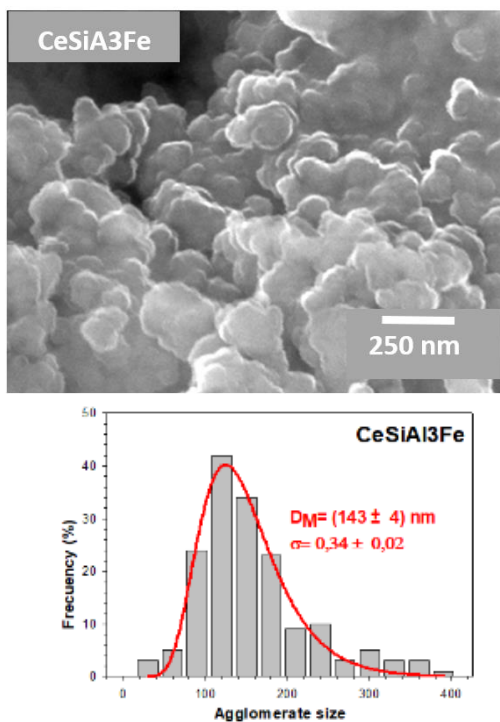
Fig. 8. SEM Images of CeSiAl3Fe sample taken in SEI mode with its respective agglomerate size distribution histogram.

Regardless compound stoichiometry, it is observed that powders are constituted by different geometry agglomerates whose sizes varied from 100 to 800 nm (table 4). These agglomerates contain smaller particles, which enclose crystallites as was discussed in XRD section. In the case of undoped CeO_2, smaller spherical particles are detailed (~700 nm) but they are even smaller for doped cerianites CeSi, CeSiAl, CeSiFe, CeSi3AlFe and CeSiAl3Fe (100 – 500 nm). From histogram results reported in table 4, it is notorious that S_p decreases with addition of dopant elements. All samples obey to logarithmic normal size distribution, typical of the sol - gel chemical route synthesis [64]. EDX chemical reveals the presence of the dopant elements in atomic percentage on ceria particles and empirical formulas were calculated from these values, in accordance with general compositions in table 1.

These results are similar to those found by Zarkov et al. [28] and Rana et al. [38] who synthesized CeO_2 nanoparticles doped with gadolinium and neodymium, respectively.

Table 3. Chemical formulas of the powders synthesized via sol - gel calculated by EDS analyses

THEORICAL FORMULA	CHEMICAL FORMULA	AGGLOMERATE SIZE (S_A), (NM)
CeO_2	$CeO_{1,98}$	791 ± 22
CeSi	$Ce_{0,59}Si_{0,41}O_{1,88}$	225 ± 17
CeSiAl	$Ce_{0,33}Si_{0,45}Al_{0,22}O_{1,60}$	160 ± 2
CeSiFe	$Ce_{0,47}Si_{0,46}Fe_{0,07}O_{1,62}$	113 ± 2
CeSi3AlFe	$Ce_{0,73}Si_{0,17}Al_{0,12}Fe_{0,01}O_{1,55}$	477 ± 32
CeSiAl3Fe	$Ce_{0,51}Si_{0,35}Al_{0,10}Fe_{0,05}O_{1,77}$	143 ± 4

Transmission Electron Microscopy

Figures 914 present TEM bright-fields images of doped and undoped ceria powders. The morphology of ceria nanoparticles mainly consists of uniform and hexagonal fine particles samples with size of ~20-25 nm.

Doped ones are spherical with a particle size in the range of 2-4 nm, in good agreement with crystallite size observed by XRD. These results are in consistent with Zhang et al [49].
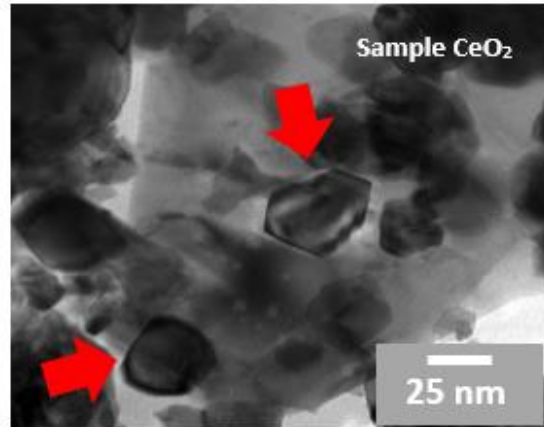
Fig. 9. TEM Images of CeO2 sample
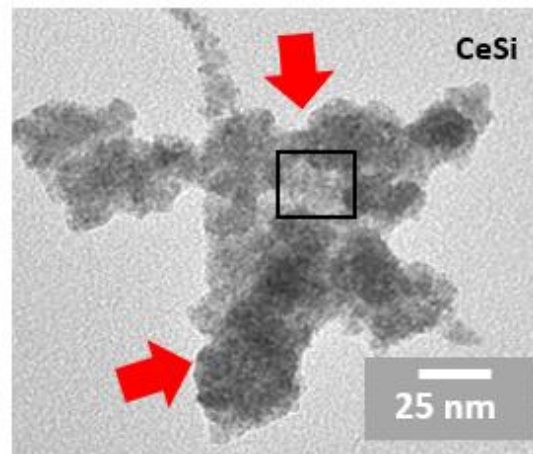
Fig. 10. TEM Images of CeSi sample.
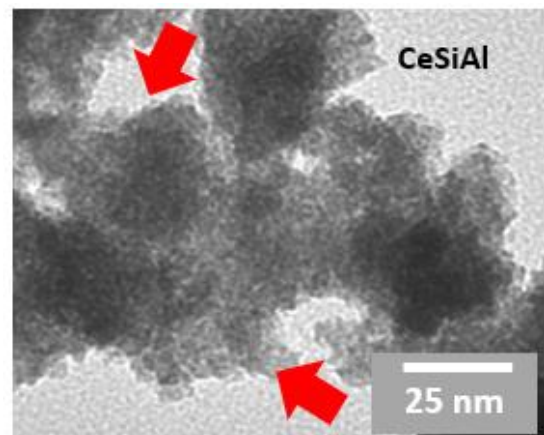
Fig. 11. TEM Images of CeSiAl sample.
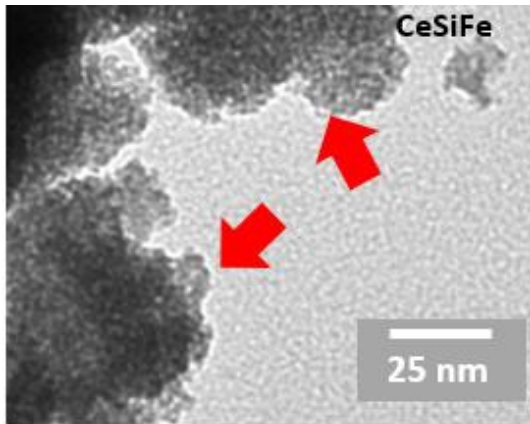
Fig. 12. TEM Images of CeSiAl sample.
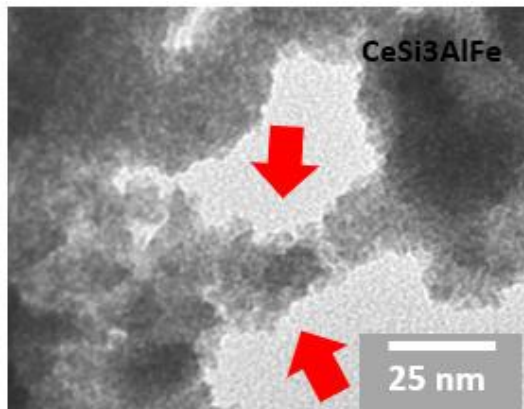
Fig. 13. TEM Images of CeSi3AlFe sample.
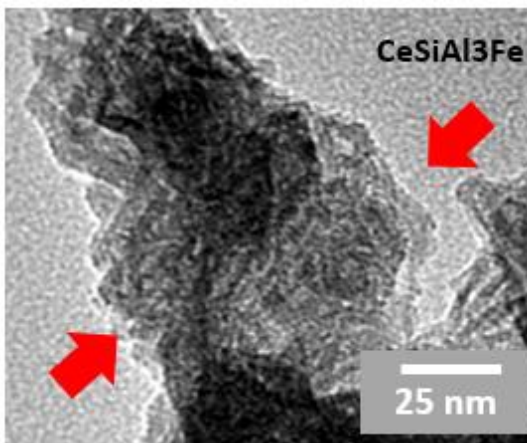
Fig. 14. TEM Images of CeSiAl3Fe sample.

SINTERED SAMPLES CHARACTERIZATION RESULTS AND DISCUSSION

X-ray diffraction

Figure 15 shows XRD patterns of doped and undoped ceria pellets obtained after conforming and sintering process at 1250 ° C. The lattice parameter value (*a*) was calculated and the results are presented in Table 4. It was observed that regardless of the doping element, all peaks match well with those of undoped sintered CeO_2 sample and there are no additional reflections that could indicate the formation of an additional phase after the sintering process. The lattice parameter decreases with the addition of the doping elements, as expected according to Vegard's law, corroborating again the introduction of the doping elements.
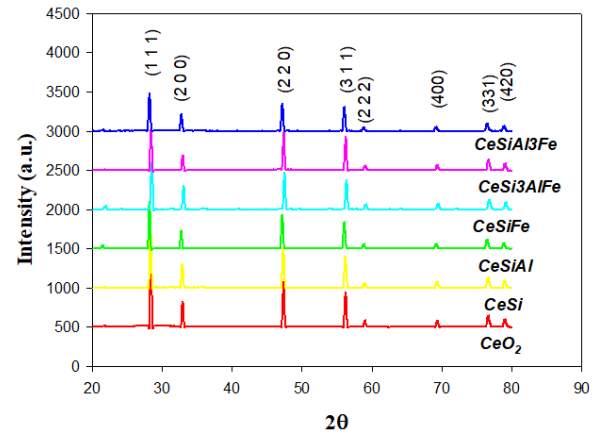
Fig. 15. Powder X-ray diffraction patterns CeO_2 and doped electrolytes: CeSi, CeSiAl, CeSiFe, CeSi3AlFe and CeSiAl3Fe.

Table 4. Chemical formulas of the powders synthesized via sol - gel calculated by EDS analyses

SAMPLE	CHEMICAL FORMULA AGGLOMERATE SIZE (S_A), (NM)
CeO_2	5.4202 ± 0.0092
CeSi	5.4196 ± 0.0039
CeSiAl	5.3996 ± 0.0055
CeSiFe	5.4080 ± 0.0017
CeSi3AlFe	5.4157 ± 0.0022
CeSiAl3Fe	5.4097 ± 0.0190

Scanning Electron Microscopy

Figures 16 to Figure 21 shows SEM images of undoped and doped sintered samples at 1250 °C during 12h. Their grain size (G), relative porosity *(RP)* and relative density *(RD)* values is also presented in table 5
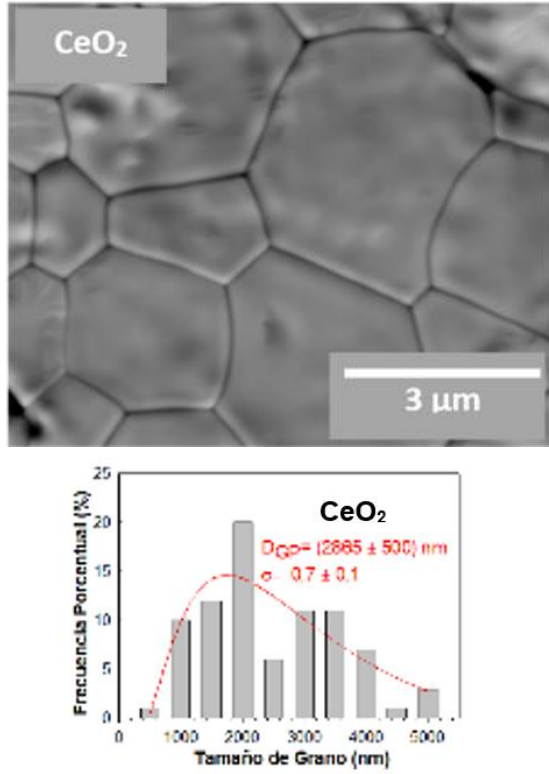
Fig. 16. SEM images of CeO₂ samples, sintered at 1250 ° C for 12 h, obtained in BSE mode inset shows gran size histogram.

Fig. 17. SEM images of CeSi samples, sintered at 1250 ° C for 12 h, obtained in BSE mode inset shows gran size histogram.
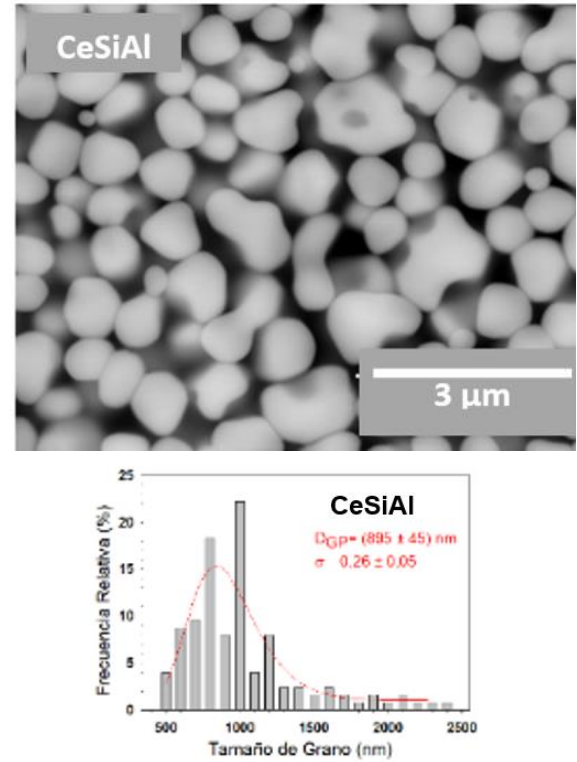
Fig. 18. SEM images of CeSiFe samples, sintered at 1250 ° C for 12 h, obtained in BSE mode inset shows gran size histogram.
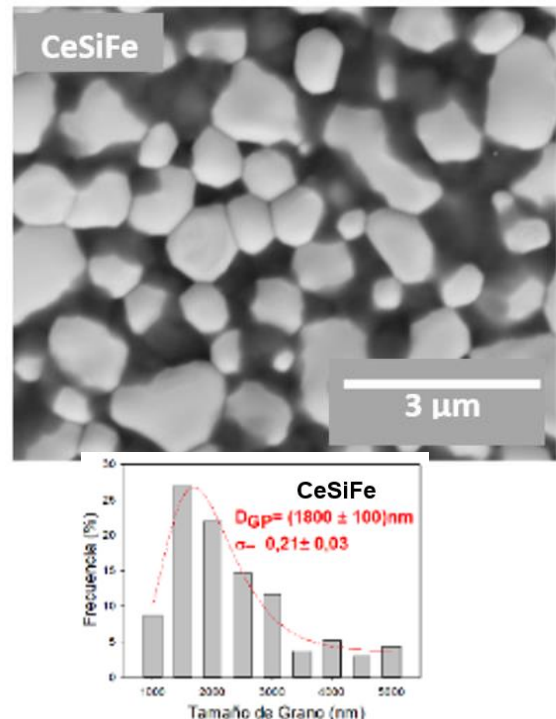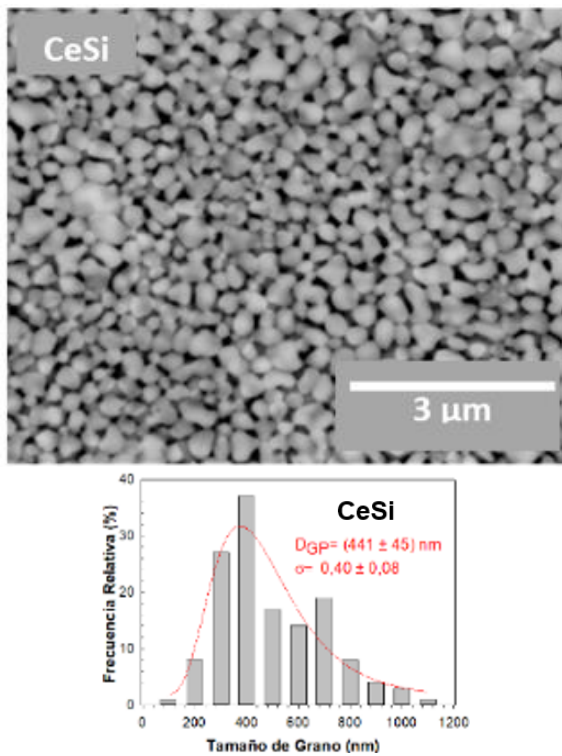
Fig. 19. SEM images of CeSiFe samples, sintered at 1250 ° C for 12 h, obtained in BSE mode inset shows gran size histogram.
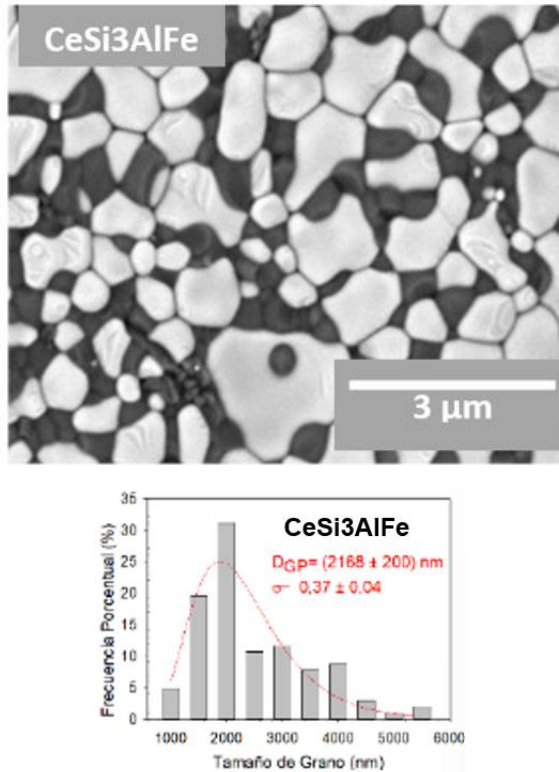
Fig. 20. SEM images of CeSi3AlFe samples, sintered at 1250 ° C for 12 h, obtained in BSE mode inset shows gran size histogram.
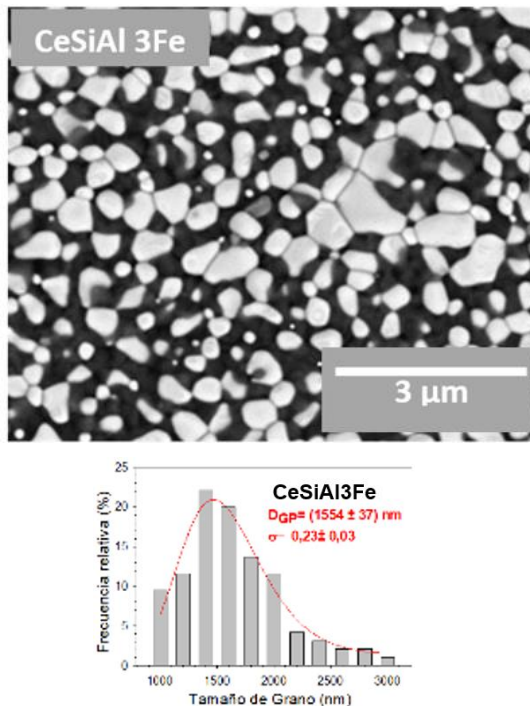
Fig. 21. SEM images of CeSiAl3Fe samples, sintered at 1250 ° C for 12 h, obtained in BSE mode inset shows gran size histogram

Figures 16 to Figure 21 shows SEM images of undoped and doped sintered samples at 1250 °C during 12h. Their grain size (G), relative porosity *(RP)* and relative density (*RD*) values is also presented in table 5 and table 6.

CeO_2 sample only shows a single phase while doped samples have three different coexisting regions: a gray diffused zone rich in Si and Fe elements, a white zone rich in Ce and Al elements and a dark zone attributed to sample porosity. Proportions and chemical composition of the different regions were calculated by EDX (table 7 and table 8). Additionally, it was observed a reduction of *G, RP* and *RD* values for doped ceria samples compared with undoped ceria.

The appearance of different coexisting regions in SEM images for doped samples could be attributed to the segregation phenomena called solute drag effect [21,65–67]. In this model, impurity solid solution atoms have a tendency of segregation to grain boundaries, an effect that may strongly retard the grain boundary mobility and thus the kinetics of recrystallization [68]. This effect causes a phase interface during phase transformations were each of these phases often have different compositions [68–70]. In XRD section it was mentioned the presence of one single crystalline structure (fluorite), but the appearance of regions forming an interface is due to a different segregation of trivalent cations in CeO_2 structure which promote inhomogeneities zones with the same crystallographic structure [21,71]. Fei et al [71] observed compositional and valence state elemental differences in Tb doped cerias and consider it a positive fact because with segregation of trivalent cations, oxygen vacancies are enriched in the domains and form an ordered structure [71]. Grain size decrease *G* could be attributed to doped elements, as Si and Al, that suppress the grain boundary mobility and retard the kinetics of mass transport during

sintering [72]. Zhang et col [73] investigation supports these results.

Grain size decrease *G* could be attributed to doped elements, as Si and Al, that suppress the grain boundary mobility and retard the kinetics of mass transport during sintering [72]. Zhang et col [73] investigation supports these results.

It is also noted that CeSi, CeSiAl and CeSiFe samples have low coalescence between the grains, which probably is reflected on decrease *RP* and *RD* values. It is possible that sintering temperature (T_S) may not have been effective at all, but the use of metal oxides (Al, Fe, Si) justifies it because they are adequate sintering aids [74,75]. Nevertheless, Ahmad et al [76] explain that T_S most used for these systems are 1300 and 1400 °C to obtain better values of densification, Jung and col [77] recommend improved the pressing and conforming processes to solve the lack of coalescence mentioned above [78].

Table 5. Grain size value (G), relative porosity (*RP*) and relative density (RD) of samples sintered at 1250 ° C

SAMPLES	GRAIN SIZE G (NM)	RELATIVE POROSITY RP (%)
CeO_2	2330 ± 80	$1,9 \pm 0,3$
CeSi	441 ± 45	$2,9 \pm 0,7$
CeSiAl	895 ± 50	$2,8 \pm 0,5$
CeSiFe	2039 ± 100	$3,9 \pm 0,2$
CeSi3AlFe	2168 ± 100	$2,6 \pm 0,6$
CeSiAl3Fe	1554 ± 90	$2,3 \pm 0,1$

Table 6. Grain size value (G), relative porosity (*RP*) and relative density (RD) of samples sintered at 1250 ° C

SAMPLE	RELATIVE DENSITY RD (%)
CeO_2	$98,2 \pm 0,3$
CeSi	94 ± 1
CeSiAl	95 ± 1
CeSiFe	93 ± 1
CeSi3AlFe	$96,6 \pm 0,2$
CeSiAl3Fe	98 ± 1

Table 7. Black phase percentages of solid sintered samples at 1250 ° C

SAMPLES	BLACK DOMAIN FORMULA	%PHASE
CeO_2	-	-
CeSi	$Ce_{0.39}Si_{0.70}O_{1.64}$	26 ± 9
CeSiAl	$Ce_{0.49}Si_{0.48}Al_{0.03}O_{1.47}$	14 ± 5
CeSiFe	$Ce_{0.65}Si_{0.13}Fe_{0.22}O_{1.51}$	19 ± 11
CeSi3AlFe	$Ce_{0.02}Si_{0.17}Al_{0.01}Fe_{0.80}O_{1.18}$	11 ± 4
CeSiAl3Fe	$Ce_{0.28}Si_{0.37}Al_{0.04}Fe_{0.44}O_{1.59}$	20 ± 7

Table 8. White phase percentages of solid sintered samples at 1250 ° C

SAMPLES	WHITE DOMAIN FORMULA	%PHASE
CeO_2	$CeO_{1.95}$	100
CeSi	$Ce_{0.63}Si_{0.25}O_{1.88}$	74 ± 9
CeSiAl	$Ce_{0.60}Si_{0.33}Al_{0.07}O_{1.90}$	86 ± 5
CeSiFe	$Ce_{0.65}Si_{0.11}Fe_{0.23}O_{1.44}$	81 ± 11
CeSi3AlFe	$Ce_{0.06}Si_{0.12}Al_{0.03}Fe_{0.79}O_{1.32}$	89 ± 4
CeSiAl3Fe	$Ce_{0.32}Si_{0.38}Al_{0.04}Fe_{0.31}O_{1.67}$	80 ± 7

Transmission Electron Microscopy

High annular dark field analysis (HADF) was carried out in CeSiAl and CeSiFe samples and the compositional mappings are presented in Figure 22 and Figure 23. It can be clearly observed that what appeared to be an absence of coalescence (pores) in the SEM images are actually grains, where cerium, oxygen, silicium, aluminum and iron distribution depending on the nature of the sample; for CeSiAl sample, silicon (denoted as dark blue) is distributed preferentially in what in the HAADF images is black.
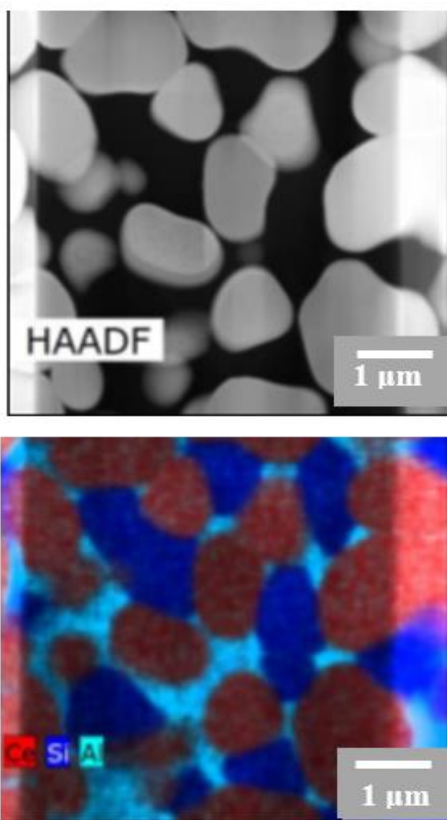
Fig. 22. HAADF and Mapping image of the CeSiAl sample in HAADF mode.
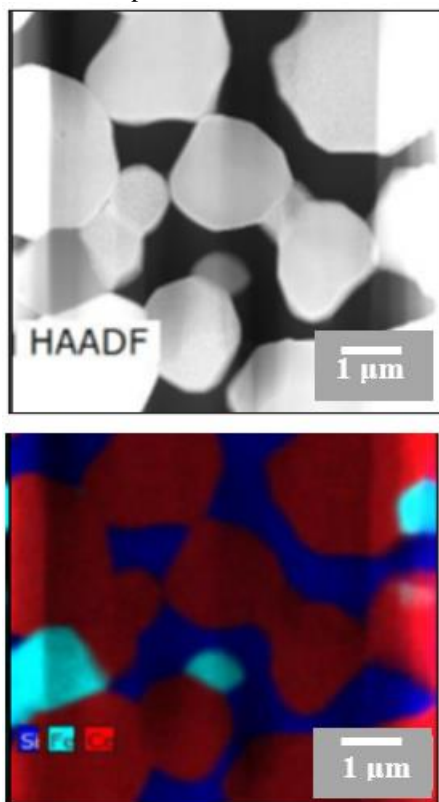
Fig. 23. HAADF and Mapping image of the CeSiFe sample in HAADF mode.

Oxygen (denoted as purple) is distributed along the entire matrix, while cerium is mostly located in the white colored areas of the HAADF mode and aluminum (denoted as light blue) is found in greater proportion. When all the colors are superimposed, three phases are observed. The same trend is observed for the CeSiFe sample. Consequently, the doping elements were introduced in CeO_2 structure in a substitutional position, but without modifying the host network. However, the proportion of each is different at each stage, indicating again trivalent cations segregation phenomena in CeO_2 structure [67,79–81].

These results agree with those observed in the investigations of Yei et al.[71] with holmium-doped ceria and in the studies of Rong Ou et al.[21] with terbium-doped ceria, originating these inhomogeneous zones. Moreover, a study of zirconium-doped ceria[82], showed a phase separation with Ce and Zr enriched regions, specifically at sintering temperatures between 1000 and 1200°C, similar to our study.

The formation of the samples could be summarized as a multi-step process, beginning with the synthesis of ceria nanoparticles via the sol-gel method. During sol-gel processing, precursors are hydrolyzed and polymerized to form a sol, which is then subjected to gelation to form a solid gel network [36,83,84]. Subsequent thermal treatment leads to the formation of ceria nanoparticles [27,49]. Following synthesis, the samples undergo sintering, where they are heated to high temperatures to promote particle rearrangement and densification [85–87]. During sintering, the dopants, such as Al and Fe, play a crucial role. These dopants diffuse into the ceria lattice, modifying its structure and reducing the activation energy for sintering [88,89]. Consequently, the sintering process occurs more efficiently, resulting in denser and more compact materials. Additionally, doping with Al and Fe leads to a decrease in particle size due to the inhibition of grain

growth during sintering, resulting in finer microstructures and improved properties [90,91]. Thus, the combination of sol-gel synthesis, doping, and sintering enables the production of high-quality ceria-based materials with enhanced performance for various applications [92].

CONCLUSIONS

To obtain Ceria nanoparticles doped with aliovalents element were obtained with a particle size in the range of 5-10 nm. The XRD analysis showed a fluorite structure as the only phase present, changes in crystal size, lattice parameter and stoichiometry of doped samples were attributed to the presence of the doping elements into ceria lattice. Sintering at 1250°C/12h showed a decrease in grain size (G) with doping and density values in the order of 0-90%. Low coalescence (RD) can be improved by increasing the sintering temperature. A segregation effect called Model Drag Solute was observed SEM and TEM. According to these results, these materials could be analyzed by electrical techniques and check their application as a precursor of solid oxide fuel cells electrodes or sensors.

REFERENCES

[1]   Morales M, R. J. J. Propiedades Mecánicas a Escala Nanometricas de YSZ y GDC usados como electrolitos en pilas de combustible de oxido sólido. *Anales de Mecánica de la Fractura* **2**, 406–410 (2009).

[2]   Talebi, T., Haji, M. & Raissi, B. Effect of sintering temperature on the microstructure, roughness and electrochemical impedance of electrophoretically deposited YSZ electrolyte for SOFCs. *Int J Hydrogen Energy* **35**, 9420–9426 (2010).

[3]   Molina, A., Campos, M. & Gonzalez, G. Caracterización de Electrolitos YSZ-SDC obtenidos a partie de polvos naométricos sintetizados por combustion. *Revista Latinoamericana de Materiales y Metalurgia* **37**, 93–101 (2017).

[4]   Castro, A. "Conformado y sinterización de mezclas de YSZ/SDC a ser utilizadas como electrolito sólido de celdas de combustible". (2009).

[5]   Wanzenberg, E., Tietz, F., Kek, D., Panjan, P. & Stöver, D. Influence of electrode contacts on conductivity measurements of thin YSZ electrolyte films and the impact on solid oxide fuel cells. *Solid State Ion* **164**, 121–129 (2003).

[6]   Wanzenberg, E., Tietz, F., Kek, D., Panjan, P. & Stöver, D. Influence of electrode contacts on conductivity measurements of thin YSZ electrolyte films and the impact on solid oxide fuel cells. *Solid State Ion* **164**, 121–129 (2003).

[7]   Kharton, V. V., Marques, F. M. B. & Atkinson, A. Transport properties of solid oxide electrolyte ceramics: A brief review. *Solid State Ion* **174**, 135–149 (2004).

[8]   Badwal, S. P. S. *Stability of Solid Oxide Fuel Cell Components. Solid State Ionics* vol. 143 www.elsevier.comrlocaterssi (2001).

[9]   Butz, B. *et al.* Correlation between microstructure and degradation in conductivity for cubic Y2O3-doped ZrO2. *Solid State Ion* **177**, 3275–3284 (2006).

[10]   Molenda, J., Świerczek, K. & Zajac, W. 'Functional materials for the IT-SOFC'. *J Power Sources* **173**, 657–670 (2007).

[11]   Mizutani, Y., Tamura, M., Kawai, M. & Yamamoto, O. Development of high-performance electrolyte in SOFC. *Solid State Ion* **72**, 271–275 (1994).

[12]   Morris, V. N., Farrell, R. A., Sexton, A. M. & Morris, M. A. Lattice Constant Dependence on Particle Size for Ceria prepared from a Citrate Sol-Gel. *J Phys Conf Ser* **26**, 119–122 (2006).

[13]   Fornasiero, P. *et al.* 'Rh-Loaded CeO2-ZrO2 Solid Solution as Highly Efficient Oxygen Exchangers: Dependende of the Reduction Behavior and the Oxygen Storage Capacity on the Structural Properties'. *J Catal* **151**, 168–177 (1995).

[14]   Vanpoucke, D. E. P., Bultinck, P., Cottenier, S., van Speybroeck, V. & van Driessche, I. 'Aliovalent doping of CeO 2: DFT study of oxidation state and vacancy effects'. *J Mater Chem A Mater* **2**, 13723 (2014).

[15]   Ouzaouit, K. *et al.* 'The influence of synthesis way and dopant on the crystallites size of ceria'. *Journal de Physique IV (Proceedings)* **123**, 125–130 (2005).

[16]   Gnanam, S. & Rajendran, V. Synthesis of CeO2 or α-Mn2O3 nanoparticles via sol-gel process and their optical properties. *J Solgel Sci Technol* **58**, 62–69 (2011).

[17]   Hong, S. J., Mehta, K. & Virkar, A. V. Effect of Microstructure and Composition on Ionic Conductivity of Rare-Earth Oxide-Doped Ceria. *Journal Electrochemical Society:* **145**, 638–647 (1998).

[18]   Herman, B. G. *et al. Effect of Microstructure and Composition on Ionic Conductivity of Rare-Earth Oxide-Doped Ceria. Inc. ner, Sens. Actuators* vol. 145 (1998).

[19] Coduri, M., Checchia, S., Longhi, M., Ceresoli, D. & Scavini, M. Rare earth doped ceria: The complex connection between structure and properties. *Front Chem* **6**, 1–23 (2018).

[20] Bjørk, R., Tikare, V., Frandsen, H. L. & Pryds, N. The effect of particle size distributions on the microstructural evolution during sintering. *Journal of the American Ceramic Society* **96**, 103–110 (2013).

[21] Ou, D. R. *et al.* Microstructural Inhomogeneity in Holmium-Doped Ceria and Its Influence on the Ionic Conduction. *J Electrochem Soc* **154**, B616 (2007).

[22] Hong, T., Zhang, Y. & Brinkman, K. Enhanced Oxygen Electrocatalysis in Heterostructured Ceria Electrolytes for Intermediate-Temperature Solid Oxide Fuel Cells. *ACS Omega* **3**, 13559–13566 (2018).

[23] Zhang, T. S., Ma, J., Chan, S. H., Hing, P. & Kilner, J. A. Intermediate-temperature ionic conductivity of ceria-based solid solutions as a function of gadolinia and silica contents. *Solid State Sci* **6**, 565–572 (2004).

[24] Zhang, T. S., Ma, J., Chan, S. H., Hing, P. & Kilner, J. A. Intermediate-temperature ionic conductivity of ceria-based solid solutions as a function of gadolinia and silica contents. *Solid State Sci* **6**, 565–572 (2004).

[25] Zheng, X. *et al.* Synthesis, characterization and catalytic property of ceria spherical nanocrystals. *Mater Lett* **59**, 2769–2773 (2005).

[26] Laberty-Robert, C. *et al.* Sol-gel-derived ceria nanoarchitectures: Synthesis, characterization, and electrical properties. *Chemistry of Materials* **18**, 50–58 (2006).

[27] Ansari, A. A. *et al.* Synthesis, structural and optical properties of Mn-doped ceria nanoparticles: A promising catalytic material. *Acta Metallurgica Sinica (English Letters)* **29**, 265–273 (2016).

[28] Zarkov, A. *et al.* Synthesis of nanocrystalline gadolinium doped ceria via sol-gel combustion and sol-gel synthesis routes. *Ceram Int* **42**, 3972–3988 (2016).

[29] Zhang, T., Hing, P., Huang, H. & Kilner, J. Sintering and grain growth of CoO-doped CeO2 ceramics. *J Eur Ceram Soc* **22**, 27–34 (2002).

[30] Farahmandjou, M. & Zarinkamar, M. 'Synthesis of nano-sized ceria (CeO2) particles via a cerium hydroxy carbonate precursor and the effect of reaction temperature on particle morphology'. *Journal of Ultrafine Grained and Nanostructured Materials* **48**, 5–10 (2015).

[31] Tok, A., Boey, F., Dong, Z. & Sun, X. 'Hydrothermal synthesis of CeO2 nano-particles'. *J Mater Process Technol* **190**, 217–222 (2007).

[32] Goulart, C. & Djurado, E. 'Synthesis and sintering of Gd-doped CeO2 nanopowders prepared by ultrasonic spray pyrolysis'. *J Eur Ceram Soc* **33**, 769–778 (2013).

[33] Masui, T. *et al.* 'Characterization of Cerium(IV) Oxide Ultrafine Particles Prepared Using Reversed Micelles'. *Chemistry of Materials* **9**, 2197–2204 (1997).

[34] Guo, J., Xin, X., Zhang, X. & Zhang, S. 'Ultrasonic-induced synthesis of high surface area colloids CeO2-ZrO2'. *Journal of Nanoparticle Research* **11**, 737–741 (2009).

[35] Kareiva, A. 'Aqueous sol-gel synthesis methods for the preparation of garnet crystal structure compounds'. *Materials Science (Medžiagotyra)* **17**, 428–437 (2011).

[36] Jung, G. B., Huang, T. J., Huang, M. H. & Chang, C. L. 'Preparation of samaria-doped ceria for solid-oxide fuel cell electrolyte by a modified sol-gel method'. *J Mater Sci* **36**, 5839–5844 (2001).

[37] Agrafiotis, C. *et al.* 'Evaluation of sol-gel methods for the synthesis of doped-ceria environmental catalysis systems. Part I: Preparation of coatings'. *J Eur Ceram Soc* **22**, 15–25 (2002).

[38] Rana, M. A. *et al. Sol-Gel Fabrication of Novel Electrolytes Based on Neodymium Doped Ceria for Application in Low Temperature Solid Oxide Fuel Cells. Materials Today: Proceedings* vol. 2 (Elsevier Ltd., 2015).

[39] Alvarado Flores J. 'Materiales para ánodos, cátodos y electrolitos utilizados en celdas óxidos de combustible de sólido (SOFC)'. *Revista Mexicana de Física* **59**, 66–87 (2013).

[40] Marne, U. De. Elaboration et caractérisation d ' un nouvel électrolyte solide pour les piles à combustible : (2004).

[41] González, M. Nuevos conductores iónicos para pilas de combustible de óxido sólido: síntesis, caracterización y propiedades eléctricas de los sistemas $Sr_2MNb_{1-x}Ti_xO_{6-x}$ /2 y $M_{2-x}(Ca,Sr)_xMgTiO_{6-x}$ /2 (M=La, Nd, Eu, Y, Gd, Yb, Lu). (2013).

[42] Arabaci, A. & Öksüzömer, M. F. Ionic conductivity of Ce0.9-xGd0.1SmxO2-δ co-doped ceria electrolytes. *Acta Phys Pol A* **134**, 122–124 (2018).

[43] Arunkumar, P., Preethi, S. & Suresh Babu, K. Role of iron addition on grain boundary conductivity of pure and samarium doped cerium oxide. *RSC Adv* **4**, 44367–44376 (2014).

[44] Dong, Q., Yin, S., Guo, C. & Sato, T. *Aluminum-Doped Ceria-Zirconia Solid Solutions with Enhanced Thermal Stability and High Oxygen Storage Capacity.* http://www.nanoscalereslett.com/content/7/1/542 (2012).

[45] Rocchini, E. *et al.* Relationships between structural/morphological modifications and oxygen storage-redox behavior of silica-doped ceria. *J Catal* **194**, 461–478 (2000).

[46] Ramesh, S., Raju, K. C. J. & Reddy, C. V. 'Synthesis and Characterization of Co-Doped Ceria Ceramics by Sol-Gel Method'. *The Indian Ceramic Society* **70**, 143–147 (2011).

[47] CelRef software.

[48] ImageJ software.

[49] Zhang, F. *et al.* Cerium oxide nanoparticles: Size-selective formation and structure analysis. *Appl Phys Lett* **80**, 127–129 (2002).

[50] Bueno-Ferrer, C., Parres-Esclapez, S., Lozano-Castelló, D. & Bueno-López, A. 'Relationship between surface area and crystal size of pure and doped cerium oxides'. *Journal of Rare Earths* **28**, 647–653 (2010).

[51] Yang, J. *et al.* Synthesis and properties of ceria based electrolyte for IT-SOFCs. *Int J Hydrogen Energy* **41**, 15979–15984 (2016).

[52] Dong, Q., Yin, S., Guo, C. & Sato, T. Aluminum-doped ceria-zirconia solid solutions with enhanced thermal stability and high oxygen storage capacity. *Nanoscale Res Lett* **7**, 542 (2012).

[53] Minervini, L. Defect cluster formation in M2O3-doped CeO2. *Solid State Ion* **116**, 339–349 (1999).

[54] Nolan, M., Fearon, J. E. & Watson, G. W. Oxygen vacancy formation and migration in ceria. *Solid State Ion* **177**, 3069–3074 (2006).

[55] Li, J. G., Ikegami, T. & Mori, T. Low temperature processing of dense samarium-doped CeO2 ceramics: Sintering and grain growth behaviors. *Acta Mater* **52**, 2221–2228 (2004).

[56] K. T. Jacob, Shubhra Raj, L. R. Vegard's law : a fundamental relation. *International Journal of Materials Research* **98**, 776–779 (2007).

[57] Dhannia, T., Jayalekshmi, S., Santhosh Kumar, M. C., Prasada Rao, T. & Chandra Bose, A. Effect of aluminium doping and annealing on structural and optical properties of cerium oxide nanocrystals. *Journal of Physics and Chemistry of Solids* **70**, 1443–1447 (2009).

[58] Rodenbough, P. P. Crystallite Size Dependency of the Pressure and Temperature Response in Nanoparticles of Ceria and Other Oxides. (Columbia University, 2016). doi:10.7916/D8QN66WH.

[59] Zhou, X. D. & Huebner, W. Size-induced lattice relaxation in CeO2 nanoparticles. *Appl Phys Lett* **79**, 3512–3514 (2001).

[60] Bryan, J. D., Schwartz, D. A. & Gamelin, D. R. Critical Nucleus Size, Composition, and Energetics in the Synthesis of Doped ZnO Quantum Dots. *ArXiv* 19 (2005).

[61] Min, B. K., Wallace, W. T., Santra, A. K. & Goodman, D. W. Role of defects in the nucleation and growth of Au nanoclusters on SiO2 thin films. *Journal Of Physical Chemistry B* **108**, 16339–16343 (2004).

[62] Anirban, S. & Dutta, A. Revisiting ionic conductivity of rare earth doped ceria: Dependency on different factors. *International Journal of Hydrogen Energy* vol. 45 25139–25166 Preprint at https://doi.org/10.1016/j.ijhydene.2020.06.119 (2020).

[63] Stojmenović, M. *et al.* Electrical properties of multidoped ceria. *Ceram Int* **40**, 9285–9292 (2014).

[64] Heintzenberg, J. Properties of the Log-Normal Particle Size Distribution. *Aerosol Science and Technology* **21**, 46–48 (1994).

[65] Chen, P. L. & Chen, I. W. Grain growth in CeO2: Dopant effects, defect mechanism, and solute drag. *Journal of the American Ceramic Society* vol. 79 1793–1800 Preprint at https://doi.org/10.1111/j.1151-2916.1996.tb07997.x (1996).

[66] Inaba, H., Nakajima, T. & Tagawa, H. Sintering behaviors of ceria and gadolinia-doped ceria. *Solid State Ion* **106**, 263–268 (1998).

[67] Ye, F. *et al.* Compositional and valent state inhomogeneities and ordering of oxygen vacancies in terbium-doped ceria. *J Appl Phys* **101**, (2007).

[68] Hersen, E., Marthinsen, K. & Nes, E. The effect of solute atoms on grain boundary migration, a solute pinning approach. *Metall Mater Trans A Phys Metall Mater Sci* **44**, 3364-3375. (2013).

[69] Sun, H. & Deng, C. Adapted solute drag model for impurity-controlled grain boundary motion. *J Mater Res* **29**, 1369–1375 (2014).

[70] Liu, Z. K., Ågren, J. & Suehiro, M. Thermodynamics of interfacial segregation in solute drag. *Materials Science and Engineering A* **247**, 222–228 (1998).

[71] Ye, F. *et al.* Compositional and valent state inhomogeneities and ordering of oxygen vacancies in terbium-doped ceria. *J Appl Phys* **101**, (2007).

[72] Schubert, H. *et al.* Solute effect on grain growth in ceria ceramics. *J Eur Ceram Soc* **14**, 337–341 (2003).

[73] Zhang, T. S., Ma, J., Leng, Y. J. & He, Z. M. Sintering, microstructure and grain growth of Fe-doped Ce 0.9Gd0.1O2-δ ceramics derived from oxalate coprecipitation. *J Cryst Growth* **274**, 603–611 (2005).

[74] Zhang, T. S. *et al.* Effect of transition metal oxides on densification and electrical properties of Si-containing Ce0.8Gd0.2O 2-δ ceramics. *Solid State Ion* **168**, 187–195 (2004).

[75] Zhang, T. S. *et al.* Iron oxide as an effective sintering aid and a grain boundary scavenger for ceria-based electrolytes. *Solid State Ion* **167**, 203–207 (2004).

[76] Ahmad, S. I., Koteshwar Rao, P. & Syed, I. A. Sintering temperature effect on density, structural and morphological properties of Mg- and Sr-doped ceria. *Journal of Taibah University for Science* **10**, 381–385 (2016).

[77] Jung, W. S., Park, H. S., Kang, Y. J. & Yoon, D. H. Lowering the sintering temperature of Gd-doped ceria by mechanochemical activation. *Ceram Int* **36**, 371–374 (2010).

[78] Pérez-Coll, D., Sánchez-López, E. & Mather, G. C. Influence of porosity on the bulk and grain-boundary electrical properties of Gd-doped ceria. *Solid State Ion* **181**, 1033–1042 (2010).

[79] Ou, D. R. *et al.* Evidence of Intragranular Segregation of Dopant Cations in Heavily Yttrium-Doped Ceria. *Electrochemical and Solid-State Letters* **10**, P1 (2007).

[80] Ou, D. R., Mori, T., Ye, F., Zou, J. & Drennan, J. Comparison between Y-doped ceria and Ho-doped ceria: Electrical conduction and microstructures. *Renew Energy* **33**, 197–200 (2008).

[81] Ye, F. *et al.* Compositional and structural characteristics of nano-sized domains in gadolinium-doped ceria. *Solid State Ion* **179**, 827–831 (2008).

[82] Masatomo Yashima, Hiroyuki Takashina, Masato Kakihana & Masahiro Yoshimura. Low Temperature Phase Equilibria by the Flux Method and the Metastable-Stable Phase Diagram in the Zr0,-CeO, System. *Journal of the American Ceramic Society* **77**, 1869–1874 (1954).

[83] Marques, A. C. *Sol Sol--Gel Process: An Overview Gel Process: An Overview*. (2007).

[84] Hamd, W. Elaboration par voie sol-gel et étude microstructurale de gels et de couches minces de. (2009).

[85] Lapa, C. M., de Souza, D. P. F., Figueiredo, F. M. L. & Marques, F. M. B. Two-step sintering ceria-based electrolytes. *Int J Hydrogen Energy* **35**, 2737–2741 (2010).

[86] Zhang, X. *et al.* A study on sintering aids for Sm0.2Ce0.8O1.9 electrolyte. *J Power Sources* **162**, 480–485 (2006).

[87] Xia, Y. *et al.* *] A) Sintering of Nanocrystalline CeO 2 Ceramics**. Macromol. Chem. Phys* vol. 99 (1999).

[88] Ravinder, D. *Dependence of Electrical Conductivity (a) and Activation Energy of Lithium Ferrite on Sintering Temperature and Porosity*.

[89] Li, Y., Gong, J. H., Tang, Z. L., Xie, Y. S. & Zhang, Z. T. Temperature-Independent Activation Energy for Ionic Conduction of Zirconia Based Solid Electrolytes. *Acta Physico - Chimica Sinica* **17**, 792–796 (2001).

[90] Gerhardt, R. & Nowick, A. S. *Grain-Boundary Effect in Ceria Doped with Trivalent Cations: I, Electrical Measurements*. *JOURNAL of the AMERICAN CERAMIC SOCIETY* vol. 69 (1986).

[91] Zhou, X.-D., Huebner, W., Kosacki, I. & Anderson, H. U. *Microstructure and Grain-Boundary Effect on Electrical Properties of Gadolinium-Doped Ceria*.

[92] Inaba, H. 'Ceria-based solid electrolytes'. *Solid State Ion* **83**, 1–16 (1996).